

# Thermal interaction-free ghost imaging

Shun Li,<sup>1</sup> Jing-Yang Xiao Feng,<sup>1</sup> Xiu-Qing Yang,<sup>2</sup> Xiaodong Zeng,<sup>1,3</sup> Xi-Hua Yang,<sup>1,3</sup>  
M. Al-Amri,<sup>4,5,\*</sup> and Zheng-Hong Li<sup>1,3,\*</sup>

*1 Department of Physics and Institute for Quantum Science and Technology, Shanghai University, Shanghai 200444, China.*

*2 College of Science, Inner Mongolia University of Technology, Hohhot 010051, China*

*3 Shanghai Key Laboratory of High Temperature Superconductors, Shanghai University, Shanghai 200444, China*

*4 NCQOQI, KACST, P. O. Box 6086, Riyadh 11442, Saudi Arabia*

*5 Institute of Quantum Technologies and Advanced Computing, KACST, Riyadh 11442, Saudi Arabia*

## **Abstract:**

We propose an interaction-free ghost imaging scheme based on a thermal light source. By utilizing the quantum Zeno-like effect, our approach significantly reduces the light dose absorbed by the sample, thereby effectively preventing sample damage induced by light-matter interactions. Combined with the elimination of entangled photon sources and single-photon detectors, our approach enables significantly more photons to be utilized for image reconstruction, thereby markedly enhancing image quality compared to conventional ghost imaging. We further demonstrate active suppression of background noise via controllable photon loss. Our work offers a practical and cost-effective route to non-destructive, high-quality imaging for light-sensitive samples in fields such as life sciences.

## **Introduction:**

Increasing the total photon number in the illumination field is one of the most straightforward methods to enhance image quality. However, this approach is limited by practical constraints such as light-induced sample damage. These limitations have motivated research into weak-field imaging, with quantum ghost imaging serving as a prominent example [1,2]. It utilizes non-classical correlations between entangled photon pairs and employs coincidence measurements to suppress random noise, enabling effective extraction of object information from extremely weak optical fields [3-5]. Although the image quality in quantum ghost imaging still benefits from photon accumulation, the low generation rate of

entangled photon pairs makes it impractical to significantly increase the total photon number. Moreover, the low-count-rate of single-photon detectors further limits imaging speed, resulting in an inverse relationship between acquisition time and photon count [5-7].

In addition to weak-field imaging, quantum mechanics also permits a more fundamental approach to avoid damage caused by light-matter interactions: interaction-free measurement [8-14]. Combined with the quantum Zeno effect, interaction-free measurement theoretically allows information acquisition without any physical “contact” [15-20]. This capability not only stimulates theoretical exploration of nonlocal quantum phenomena [21-24] but also holds promise for significant applications in fields such as quantum communication [25-29], quantum information processing [30-34], and quantum sensing [35-40]. Particularly for light-sensitive samples, this method offers a powerful tool for the dynamic observation of biological specimens like living cells and proteins [12,15,39]. Recently, researchers have begun exploring the combination of interaction-free measurement with quantum ghost imaging [41-43]. However, such hybrid schemes still require entangled sources and single-photon detectors, and thus fail to overcome the efficiency bottleneck inherent in quantum ghost imaging.

It is noteworthy that ghost imaging does not inherently require quantum light [44-47]. Initial work in 2002 demonstrated that ghost imaging could be performed without entanglement [48]. Building on this, a practical scheme utilizing thermal light was subsequently proposed, which operated without the need for single-photon detectors [49]. Compared to quantum ghost imaging, thermal ghost imaging consistently suffers from substantial background noise, meaning that—under the same total photon number in the illumination field—it exhibits inferior image quality [6]. However, studies also indicate that the image quality of ghost imaging is proportional to the number of measurements (denoted as  $K$ ) and the average photon number per measurement. For thermal ghost imaging, the photon count per measurement can be very high, whereas quantum ghost imaging typically uses only one photon per measurement. This allows thermal ghost imaging to achieve better image quality in a single measurement while also offering a relatively faster imaging speed [6]. In general, the two approaches are suited to different scenarios. The quantum method is more appropriate for situations with limited total photon numbers or extremely weak

illumination (where photons in the illumination field are a scarce resource). The thermal method holds an advantage when strong illumination is permissible (where photons are abundant), and its main challenges lie in the increased risk of sample damage under high light dose, as well as inherently high background noise [50].

In this work, we combine, for the first time, interaction-free measurement with thermal ghost imaging, dramatically reducing light-induced damage. This allows our approach to safely increase the number of measurements to levels unattainable by traditional thermal ghost imaging, thereby significantly improving the image quality. The study further reveals that optical loss can serve as an effective parameter for regulating background noise, offering a new dimension for actively optimizing imaging performance. Moreover, as a result of eliminating single-photon detectors and entangled sources, our scheme enables faster imaging, higher system stability, and lower cost, in contrast to quantum ghost imaging schemes that employ interaction-free measurement. It is also worth mentioning that our theoretical framework is applicable to computational ghost imaging [51-57], which evolved from thermal ghost imaging and operates on the same underlying principles.

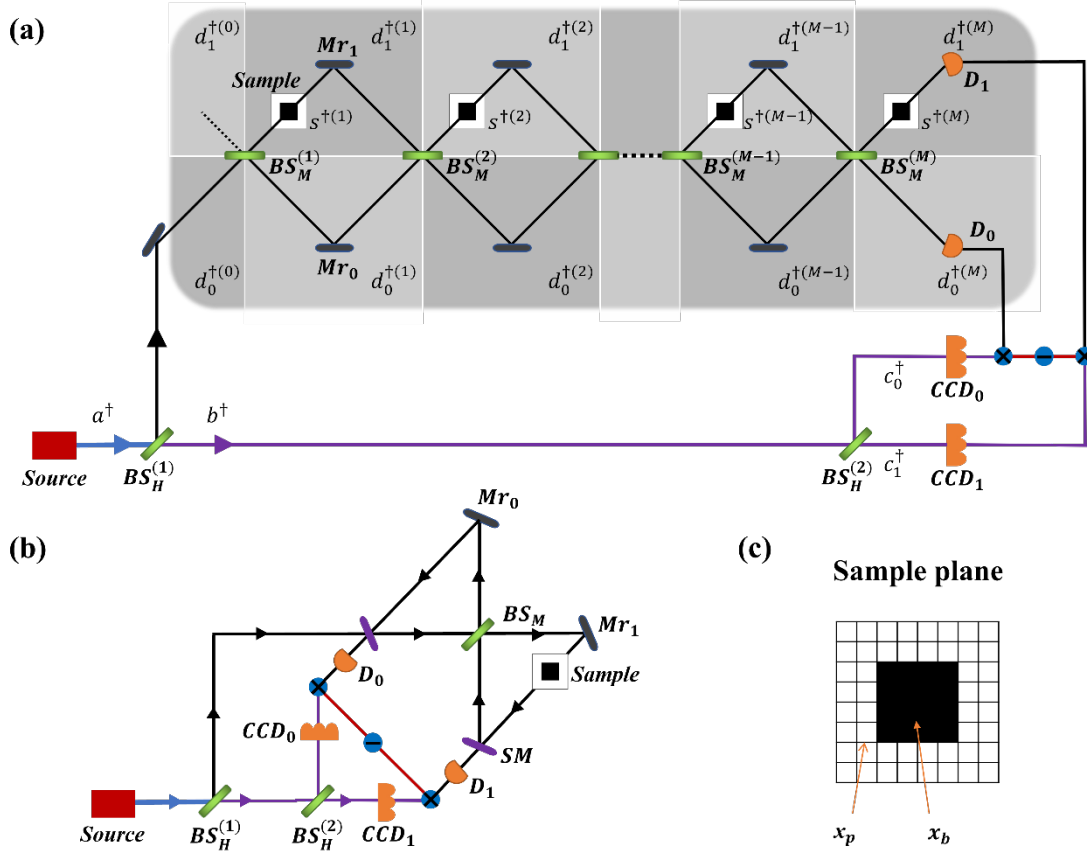


Fig. 1 Schematic of the thermal light interaction-free ghost imaging: (a) Implementation based on a chain interferometer structure; (b) Equivalent Michelson interferometer configuration; (c) Discretized model of the sample plane.

## Results:

### Basic model

Fig. 1(a) presents the thermal light interaction-free ghost imaging scheme. Our system introduces a chain interferometer structure into the signal path of the conventional approach [50], enabling multiple “interactions” between the illumination field and the sample. Thanks to this configuration, the light that would be directly absorbed by the sample in traditional schemes is now collected and directed to the non-spatially resolving bucket detector  $D_0$ , while the light transmitted through the transparent regions of the sample is guided to bucket detector  $D_1$ . The reference path is separated from the signal path by a 50:50 beam splitter  $BS_H^{(1)}$ , while a second  $BS_H^{(2)}$  evenly divides the reference light into two beams, which are then respectively sent to two *CCDs*. These undergo coincidence measurements with the two bucket detectors, and the final measurement signal is obtained through differential output.

The chain structure consists of mirrors ( $Mr$ ) and  $M$  beam splitters  $BS_M^{(m)}$  with identical reflectivity ( $\cos^2(\pi/2M)$ ), where the superscript  $m$  denotes the  $m$ -th beam splitter. When  $M = 1$ , the system reduces to the conventional thermal light ghost imaging configuration [50]. Fig. 1(b) shows the equivalent Michelson interferometer version [34] corresponding to Fig. 1(a). By using switchable mirrors ( $SM$ ), the light pulses are confined within the interferometer cavity [58], forced to interact with the sample  $M$  times in cycles before being released to the detectors. While Fig. 1(b) depicts a more practical application scenario [34], the configuration in Fig. 1(a) is better suited for theoretical analysis and experimental verification. Therefore, this paper will use Fig. 1(a) as the basis for discussion.

For simplicity, we focus on an ideal binary sample. As shown in Fig. 1(c), the sample surface is divided into  $J$  units, each uniquely identified by  $x_j$  ( $j = 1, 2, \dots, J$ ), forming the set  $\mathbf{J} = \{x_j\}$ . Each unit is either transparent (denoted as  $x_p$ , belonging to set  $\mathbf{J}_p$  with total number  $J_p$ ), allowing photon transmission, or opaque (denoted as  $x_b$ , belonging to set  $\mathbf{J}_b$  with total number  $J_b$ ). With the definition  $\alpha = J_b/J_p$ , the average transmittance of the sample is  $1/(1 + \alpha)$ . Furthermore, we assume that each sample unit matches the size of an *CCD* pixel and the average speckle size of the light source [50]. Under this configuration, the

corresponding positions in the sample plane, detection plane, and source plane maintain a one-to-one spatial correspondence, all describable by the same coordinate  $x$ .

The optical field operators and measurement processes in the system are defined as follows. Let  $a^\dagger$  denote the creation operator of the illumination field at the source plane. We assume that the light intensities in different speckles are statistically independent. The average number of photons within a single speckle per measurement is  $2u$ , i.e.,  $\langle I_a(x) \rangle = 2u$ , where  $I_a(x) = a^\dagger(x)a(x)$ . The reference beam is described by  $b^\dagger$ . After passing through  $BS_H^{(2)}$ , the creation operators of the optical fields entering the two  $CCDs$  per measurement are denoted  $c_i^\dagger$  with  $i = 0, 1$ . Correspondingly, the average number of photons detected at pixel  $x$  of  $CCD_i$  is  $I_{ci}(x) = c_i^\dagger(x)c_i(x)$ . In the chain structure of the signal path,  $d_1^{\dagger(m)}$  and  $d_0^{\dagger(m)}$  represent the creation operators of the optical fields in the upper and lower paths, respectively, between the  $m$ -th beam splitter  $BS_M^{(m)}$  and the next one. The average number of photons received by bucket detector  $D_i$  ( $i = 0, 1$ ) per measurement is  $I_i = \sum_{x \in J} d_i^{\dagger(m)}(x)d_i^{(m)}(x)$ . Additionally,  $s^{\dagger(m)}$  represents the operator associated with light absorption by the sample during the  $m$ -th interaction.

After  $K$  independent coincidence measurements between  $D_i$  and  $CCD_i$ , their statistical average is denoted as  $E[I_i I_{ci}(x)]$ . Here, the expectation operator  $E[\cdot]$  is defined as the arithmetic mean of any observable  $X$ , i.e.,  $E[X] = \sum_{k=1}^K X^{(k)} / K$ , where  $X^{(k)}$  is the value of  $X$  in the  $k$ -th measurement. It should be noted that background noise is a non-negligible factor in thermal light ghost imaging [48,49]. Here we adopt the most commonly used background subtraction method, directly subtracting the background noise term  $E[I_i]E[I_{ci}(x)]$  [59-62]. The corrected coincidence measurement result can be expressed as  $g_i(x) = E[I_i I_{ci}(x)] - E[I_i]E[I_{ci}(x)]$ . Finally, the output signal  $G$  of our scheme is defined as the difference between the corrected results from the two detection channels:

$$G(x) = g_1(x) - g_0(x). \quad (1)$$

### Computational method and expression for the sample imaging signal $\langle G(x) \rangle$

First, we clarify the relationships between the detection-end operators  $d_i^{\dagger(m)}$ ,  $c_i^\dagger$  and the source operator  $a^\dagger$ . For the  $CCD$ , it is straightforward to obtain  $c_i^\dagger(x) = a^\dagger(x)/2$  due to the two 50:50  $BS_H$ s. For the bucket detectors, we define coefficients  $\chi_{pi}$  and  $\chi_{bi}$  such that  $d_i^{\dagger(m)}(x_p) = \chi_{pi}a^\dagger(x_p)/\sqrt{2}$  for transparent units, while for opaque units,  $d_i^{\dagger(m)}(x_b) = \chi_{bi}a^\dagger(x_b)/\sqrt{2}$ . The factor  $1/\sqrt{2}$  originates from  $BS_H^{(1)}$ , while  $\chi_{pi}$  and  $\chi_{bi}$  depend on all

optical components in the chain. Regarding  $BS_M^{(m)}$ , the input and output field operators satisfy the following relations:  $d_0^{\dagger(m)} = d_0^{\dagger(m-1)} \cos \theta - d_1^{\dagger(m-1)} \sin \theta$  and  $d_1^{\dagger(m)} = d_0^{\dagger(m-1)} \sin \theta + d_1^{\dagger(m-1)} \cos \theta$  where  $\theta = \pi/(2M)$  [24]. As for the sample, transparent units leave the optical field unchanged, resulting in  $d_1^{\dagger(m)} \rightarrow d_1^{\dagger(m)}$ , while opaque units absorb and annihilate photons, leading to  $d_1^{\dagger(m)} \rightarrow 0$ . Under the condition that all other components in the optical path, such as the mirrors ( $Mr$ ), are ideal, we obtain  $\chi_{p0} = 0$ ,  $\chi_{p1} = 1$ ,  $\chi_{b1} = 0$ , and  $\chi_{b0} = \cos^M \theta$  [24,63]. As  $M$  approaches infinity,  $\chi_{b0}$  approaches 1. In our calculations, we have assumed that the incident field is sufficiently intense (i.e.,  $u$  is very large) such that shot noise can be neglected [50], and similarly, the effects of vacuum input fields are also negligible [63]. This high-intensity illumination approximation is applied in all subsequent calculations.

When the mirrors are non-ideal, we assume that the reflectivity of each  $Mr_0$  in the lower path is  $\eta_0^2$ , and the reflectivity of the  $Mr_1$  in the upper path is  $\eta_1^2$ , meaning the loss probabilities per reflection are  $\gamma_0 = 1 - \eta_0^2$  and  $\gamma_1 = 1 - \eta_1^2$ , respectively. In this case,  $\chi_{b1} = 0$  and  $\chi_{b0} = \eta_0^M \cos^M \theta$  [63]. However,  $\chi_{p0}$  and  $\chi_{p1}$  depend on  $\eta_0$  and  $\eta_1$  in a complex manner, which is better analyzed using numerical simulations. It should be noted that other optical losses in the chain structure can be uniformly modeled as the optical loss caused by  $Mr_0$  and  $Mr_1$ .

After establishing the operator relationships between the detection and source ends, we apply the Gaussian moment theorem [48,64] to calculate  $\langle G(x) \rangle$ . Under high-intensity illumination approximation, the expression of the theorem simplifies to:  $\langle I_a^n(x) \rangle = n! (2u)^n$  and  $\langle I_a(x)I_a(x') \rangle = \langle I_a(x) \rangle \langle I_a(x') \rangle = (2u)^2$ , for  $x \neq x'$  [50]. This yields the following results [63]:

$$\langle G(x_p) \rangle = \frac{K-1}{2K} C_p u^2, \quad \langle G(x_b) \rangle = -\frac{K-1}{2K} C_b u^2, \quad (2)$$

where  $C_p = |\chi_{p1}|^2 - |\chi_{p0}|^2$  and  $C_b = |\chi_{b0}|^2 - |\chi_{b1}|^2$ . When all mirrors are perfect, with  $K \gg 1$  and  $M \gg 1$ , we have  $\langle G(x_p) \rangle = -\langle G(x_b) \rangle = u^2/2$ . This confirms that our scheme effectively extracts sample information.

### Contrast-to-noise ratio (CNR)

CNR is a commonly used metric for evaluating ghost imaging performance [41-43,50], defined as:  $CNR \equiv (\langle G(x_p) \rangle - \langle G(x_b) \rangle) / \sqrt{\frac{1}{2} [\delta^2 G(x_p) + \delta^2 G(x_b)]}$ , where  $\delta^2 G \equiv \langle G^2 \rangle - \langle G \rangle^2$ . The numerator of this expression represents the unnormalized visibility, thus CNR can

be regarded as a comprehensive measure combining signal-to-noise ratio and visibility. In Supplementary Notes 3, we provide the derivation process, ultimately obtaining:

$$CNR = \frac{(c_p + c_b)\sqrt{K-1}}{\sqrt{c_p^2(J_p+7/2-3/K) + c_b^2(J_b+7/2-3/K)}}. \quad (3)$$

It is worth noting that under the condition of  $M = 1$  (with optical losses neglected, i.e.,  $\eta_0 = \eta_1 = 1$ ), we have  $c_p = 1$  and  $c_b = 0$ . In this case, Eq. (3) reduces to the known result in the traditional scheme [50].

Without loss of generality, consider the scenario where  $K$ ,  $J_p$ , and  $J_b$  are all large. The CNR of traditional thermal ghost imaging is approximately  $CNR' \approx \sqrt{K'/J_p}$ , while in our scheme,  $CNR \approx (2/\sqrt{1+\alpha})\sqrt{K/J_p}$  when  $M$  is sufficiently large. We note that the total number of photons in the illumination field is determined by both  $u$  and  $K$ . Although  $u$  is the key factor enabling thermal ghost imaging to achieve a higher imaging speed compared to quantum ghost imaging, its benefit to image quality saturates as it increases [6, 50]. In this work, due to the high-intensity illumination approximation, we are precisely in the aforementioned regime. As shown in Eq. (3),  $u$  does not appear and thus does not affect the CNR. Therefore, the impact of the total photon number can be analyzed solely through  $K$ . When  $K = K'$ , the advantage of our scheme depends on the proportion of transparent area in the sample. The higher the proportion of transparent regions, the better the CNR. It can be observed that as long as  $\alpha \leq 3$ , our scheme consistently outperforms traditional methods. For example, when the transparent and opaque areas are equal ( $\alpha = 1$ ), the CNR of our scheme can theoretically be improved to  $\sqrt{2}$  times that of the traditional scheme. The above results have an intuitive physical explanation: the very light that our scheme can utilize—light that conventional methods lose through absorption—carries inherent noise. This causes the CNR of our scheme to deteriorate relative to conventional approaches as the sample's opaque area grows.

The above analysis treats the total photon number in the illumination field as a constrained resource (thus keeping  $K$  identical in the comparison). Next, we show that relaxing this constraint allows our scheme to achieve significantly enhanced image quality.

### Enhancing CNR by increasing $K$ under fixed sample absorption

Maintaining the light dose delivered to the sample within a safety threshold is crucial for applications such as in vivo biological imaging. In traditional ghost imaging schemes, the total light absorption by the sample under ideal conditions is given by  $I'_{abs} = K'J_bu$ . In our scheme,

due to multiple interactions between the sample and the light field, the total light absorption over  $M$  interactions must be accumulated. Assuming the operators  $s^{\dagger(m)}$  and  $a^\dagger$  are related by the coefficient  $\chi_{abs}^{(m)}$ , i.e.,  $s^{\dagger(m)}(x_b) = \chi_{abs}^{(m)} a^\dagger(x_b) / \sqrt{2}$ , the total light absorption throughout the imaging process is:

$$I_{abs} = K J_b \sum_{m=1}^M \langle s^{\dagger(m)} s^{(m)} \rangle = u K J_b \sum_{m=1}^M \left| \chi_{abs}^{(m)} \right|^2. \quad (4)$$

The calculation of  $\chi_{abs}^{(m)}$  is analogous to that of  $\chi_p$  and  $\chi_b$ . Specifically, for a lossless chain structure with large  $M$ , we obtain  $I_{abs} \approx K J_b \pi^2 u / 4M$  [63], which indicates that the light absorption per measurement in our scheme is far lower than that in the traditional approach, and thus the total light dose is also significantly reduced. As  $M \rightarrow \infty$ , the absorption approaches zero. Consequently, even under intense illumination, our scheme ensures that the sample remains undamaged. The underlying principle of this phenomenon is analogous to the quantum Zeno effect: continuous observation (via sample absorption) prevents the light field from transitioning out of its initial path (the lower path), thereby significantly reducing the light dose delivered to the sample. It should be noted that for practical applications, it is not necessary to strictly ensure that the sample absorbs no photons during the measurement process (i.e., with  $M$  being infinite). Considering the condition of finite  $M$ , we refer to this as a quantum Zeno-like effect. An increase in  $M$  enhances the sample's tolerance to light-induced damage.

For the same light dose absorbed by the sample as in the traditional scheme, our scheme achieves a photon-number amplification factor of  $K/K' = 4M/\pi^2$ . This results in an approximate CNR improvement of  $CNR/CNR' \approx (4\sqrt{M})/(\pi\sqrt{1+\alpha})$ . Consequently, the image quality is proportional to  $\sqrt{M}$ , and our scheme outperforms the traditional method in image quality as long as  $M > \alpha$ .

### Enhancing CNR by exploiting controllable optical loss for noise suppression

Prior analysis assumed negligible optical loss in the chain structure. Although losses are generally thought to impair imaging by reducing interference, we next show that controlled optical loss can actually enhance performance.

To simplify the analysis, we first consider the case of large  $K$ , where Eq.(3) reduces to:

$CNR \approx \sqrt{K/J_p} (C_p + C_b) / \sqrt{C_p^2 + \alpha C_b^2}$ . By differentiating the CNR with respect to the reflection coefficient  $\eta_0$  of the lower optical path and substituting the relation  $C_b = \eta_0^{2M} \cos^{2M} \theta$  [63],

the extremum condition is found to be either  $C_p = \alpha C_b$  or  $\eta_0 \partial C_p / \partial \eta_0 = 2MC_p$ . Due to the typically large value of  $M$ , the latter condition is generally difficult to satisfy. The former condition  $C_p = \alpha C_b$ , however, leads to a vanishing photon number difference between the two bucket detectors per measurement, since  $\langle I_1 \rangle - \langle I_0 \rangle = J_p [C_p - \alpha C_b]u$  [63]. As shown in Supplementary Note 3, this quantity directly determines the difference in background noise between the two measurement channels. Thus,  $C_p = \alpha C_b$  corresponds to automatic cancellation of background noise. Under this condition and when  $\alpha > 1$ , the maximum CNR is given by:

$$CNR_{MAX} = \sqrt{\frac{K}{J_p}} \sqrt{1 + \frac{1}{\alpha}}. \quad (5)$$

Evidently, even when  $K = K'$ , the CNR upper bound in our scheme is always higher than in the traditional scheme, and  $\alpha$  ceases to be a limiting factor.

While the above results establish the theoretical CNR upper limit for our scheme, its practical advantage range under specific optical loss conditions is delineated in Fig. 2. This figure illustrates the ratio of the CNR in our scheme to that of the traditional scheme as a function of the lower-path mirror loss  $\gamma_0$  under the condition  $K = K'$ , with different colored curves representing varying levels of upper-path mirror loss  $\gamma_1$ . From Fig. 2, not only can an extremum in the CNR be observed, but it is also evident that over a wide range of  $\gamma_0$  and  $\gamma_1$  values, our scheme maintains a CNR advantage over the traditional scheme (i.e., the ratio is greater than 1). This indicates, on the one hand, that optical losses in the upper and lower paths do not severely degrade the imaging performance of our scheme; on the other hand, it suggests that by controlling optical loss, background noise can be effectively regulated, thereby enhancing image quality.

To quantitatively assess the performance gain under a fixed sample absorption—in contrast to the fixed total photon number in the illumination field considered previously—we plot in Fig. 3 the ratio of the CNR of our scheme to that of the traditional one (assuming an ideal device for the traditional scheme) as a function of  $\gamma_0$  and  $\gamma_1$ . In the simulation, we first numerically calculate the absorption coefficient  $\sum_{m=1}^M |\chi_{abs}^{(m)}|^2$ , and then determine the required number of measurements for our scheme based on the relation  $K = K' / \sum_{m=1}^M |\chi_{abs}^{(m)}|^2$ . The black regions in the figure indicate the parameter ranges where our scheme provides no advantage (i.e., CNR ratio  $\leq 1$ ). However, over a broad and practically relevant region of the parameter space, our scheme substantially outperforms the

conventional approach. The results demonstrate a highly significant performance improvement. Specifically, the imaging performance improves with increasing  $M$ . As shown in Fig. 3(b), when  $M = 10$ , the CNR of our scheme reaches 10 times that of the conventional scheme. Additionally, as shown in Figs. 3(e) and 3(f), even when  $\alpha > 3$ , our scheme can still achieve a superior CNR by tuning the optical loss. Although the improvement is less pronounced than when  $\alpha$  is small, a performance enhancement of over threefold can still be achieved across a wide range of  $\gamma_0$  and  $\gamma_1$ .

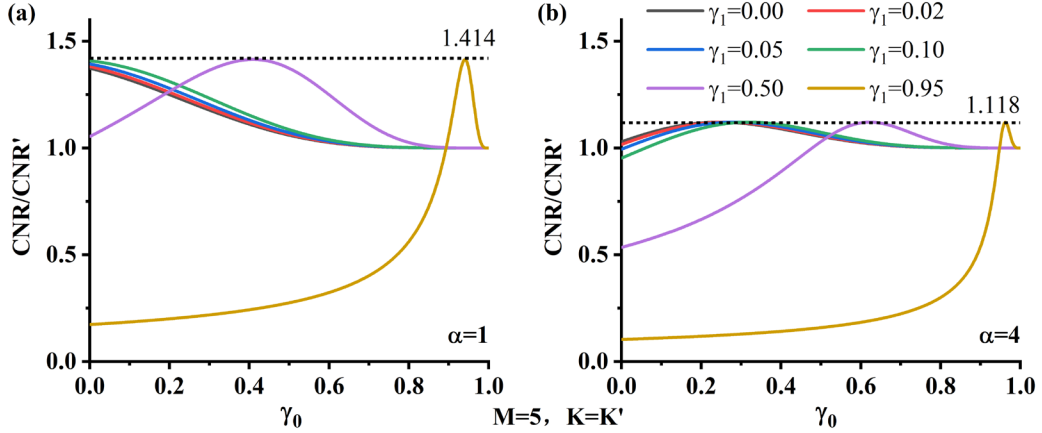


Fig. 2 Ratio of the CNR for the interaction-free scheme to that of the traditional scheme under the condition  $K = K'$ , plotted as a function of the optical loss probability  $\gamma_0$  for different  $\gamma_1$ . Panels (a) and (b) correspond to  $\alpha = 1$  and  $\alpha = 4$ , respectively.

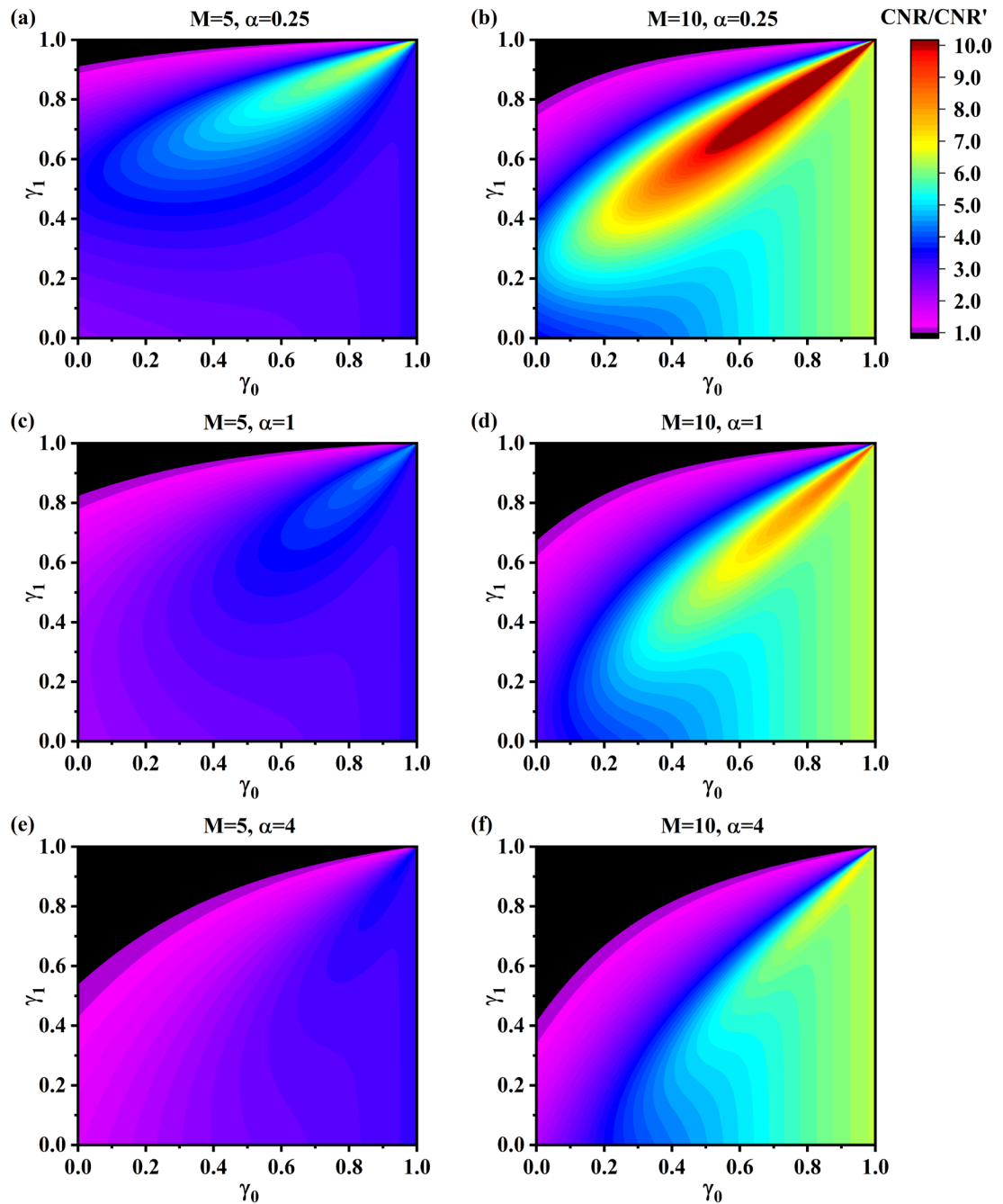


Fig. 3 Ratio of the CNR for the interaction-free scheme to that of the traditional scheme under identical absorption conditions, plotted as a function of optical loss probabilities  $\gamma_0$  and  $\gamma_1$ . The parameters ( $M$ ,  $\alpha$ ) for panels (a-f) are: (a) (5, 0.25), (b) (10, 0.25), (c) (5, 1), (d) (10, 1), (e) (5, 4), and (f) (10, 4).

#### Discussion:

##### Validity of the approximation of high-intensity illumination

Although numerical analysis confirms that increasing optical loss can enhance CNR, this enhancement is inherently limited—when optical loss continues to increase, the bucket detector will eventually fail to receive enough photons. This raises a critical issue: once the average number of photons received by the detector decreases to the point where shot noise cannot be ignored, our previous calculations are no longer valid. We therefore proceed to analyze the valid range of optical loss next.

As a reference, we first recall the experimental conditions in [50]: the bucket detector received a light pulse of approximately  $1\text{ nJ}$ , the sample transparent area was  $5\text{ mm}^2$ , and the *CCD* single-pixel area was  $10\text{ }\mu\text{m}^2$ . According to [50], each *CCD* pixel received about 7800 photons per pulse, while the bucket detector received approximately  $3.9 \times 10^9$  photons. Moreover, [50] indicates that when the number of photons received per pixel exceeds 10, shot noise can be neglected. Noting that our scheme introduces only a chain structure into the signal path compared to the traditional ghost imaging scheme, we can assume the use of the same light source as in [50] and determine whether shot noise is negligible by comparing the ratio of the photon numbers received by the detectors in the two schemes.

For the *CCD*, our scheme only adds a 50:50 beam splitter without introducing additional optical loss, so its shot noise remains negligible. We note that for the bucket detectors, the average number of photons per measurement in the traditional scheme is  $\langle I'_0 \rangle = J_p u$ . In our scheme, for  $i = 0, 1$ , the corresponding average photon number at each bucket detector is  $\langle I_i \rangle = (J_p |\chi_{pi}|^2 + J_b |\chi_{bi}|^2) u$ . Fig. 4 shows the ratio  $\langle I_i \rangle / \langle I'_0 \rangle$  as a function of optical loss. White curves for ratios of  $10^{-2}$ ,  $10^{-4}$ , and  $10^{-6}$  are also plotted (corresponding to the bucket detector in our scheme receiving  $3.9 \times 10^7$ ,  $3.9 \times 10^5$ , and  $3.9 \times 10^3$  photons, respectively). By comparing Figs. 3(c), 3(d) and Fig. 4, it can be observed that even with significant optical attenuation in the chain structure, the detectors can still capture enough photons so that shot noise can be neglected, and the CNR advantage of our scheme remains significant, demonstrating that it is feasible to substantially improve the imaging CNR by controlling optical loss.

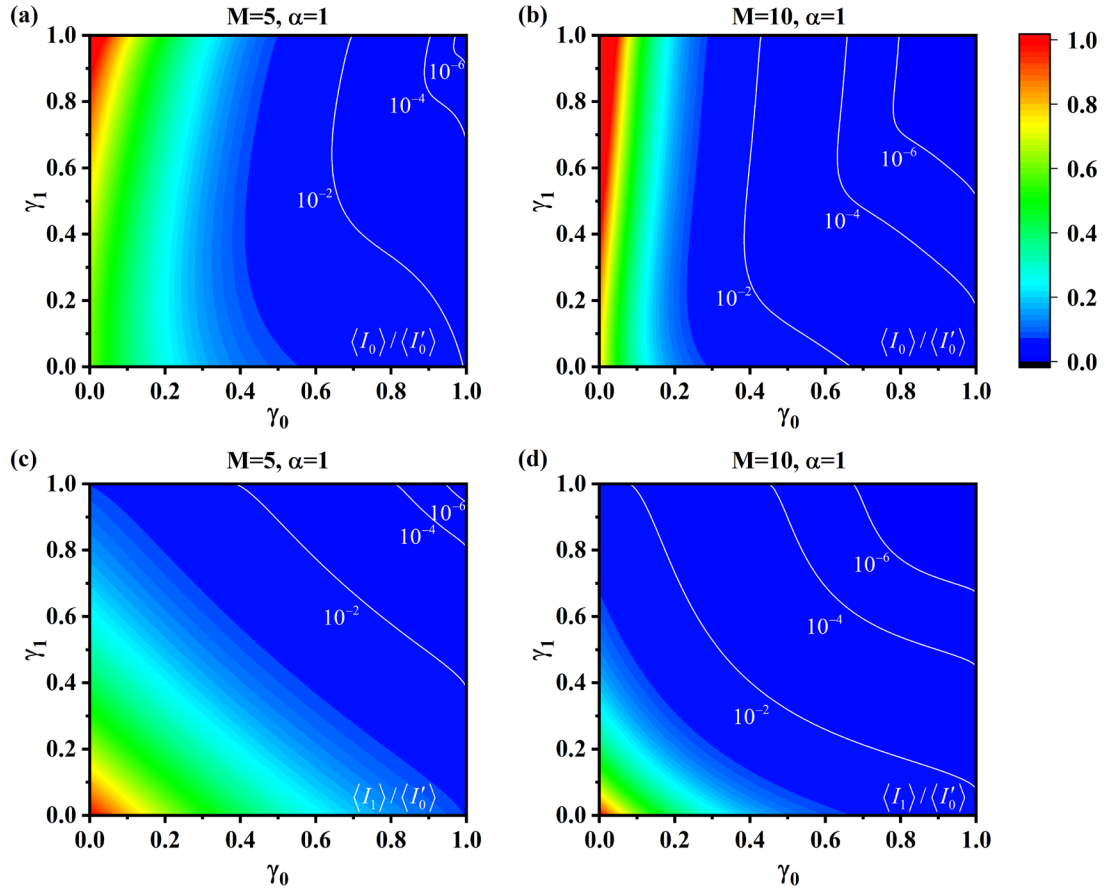


Fig. 4 Comparison of the average number of photons received by the bucket detectors per measurement in the proposed and traditional schemes for different optical loss probabilities  $\gamma_0$  and  $\gamma_1$ , with  $\alpha = 1$ . Here,  $\langle I_0 \rangle$ ,  $\langle I_1 \rangle$ ,  $\langle I'_0 \rangle$  denote the photon numbers collected by  $D_0$  (proposed scheme),  $D_1$  (proposed scheme), and the bucket detector in the traditional scheme, respectively. The plots show (a)  $\langle I_0 \rangle / \langle I'_0 \rangle$  for  $M = 5$ , (b)  $\langle I_0 \rangle / \langle I'_0 \rangle$  for  $M = 10$ , (c)  $\langle I_1 \rangle / \langle I'_0 \rangle$  for  $M = 5$ , and (d)  $\langle I_1 \rangle / \langle I'_0 \rangle$  for  $M = 10$ .

## Visibility

We now complement our analysis by adopting traditional visibility, which is defined as:

$$V = \frac{|\langle g(x_p) \rangle - \langle g(x_b) \rangle|}{\langle g_1(x_p) \rangle + \langle g_1(x_b) \rangle + \langle g_0(x_p) \rangle + \langle g_0(x_b) \rangle} = \frac{|\chi_{p1}|^2 + |\chi_{b0}|^2 - |\chi_{b1}|^2 - |\chi_{p0}|^2}{|\chi_{p1}|^2 + |\chi_{b0}|^2 + |\chi_{b1}|^2 + |\chi_{p0}|^2}, \quad (6)$$

where the denominator represents the sum of signals from both transparent and opaque sample units in the two sets of *CCD*-bucket detector coincidence measurements. Under ideal conditions, the visibility value is 1. It is worth emphasizing that this normalized visibility depends solely on the parameters of the chain structure itself, such as  $M$ ,  $\gamma_0$ , and  $\gamma_1$ , and is

independent of other variables including  $K$ ,  $u$ , and  $\alpha$ .

Fig. 5 shows the variation of visibility against optical loss probabilities  $\gamma_0$  and  $\gamma_1$ . Fig. 5(a) corresponds to  $M = 5$ , and Fig. 5(b) corresponds to  $M = 10$ . The black areas in the figure indicate regions where visibility is below 0.5. Simulation results show that even under high optical loss conditions, the system can still maintain high visibility, provided that  $\gamma_0 \approx \gamma_1$ .

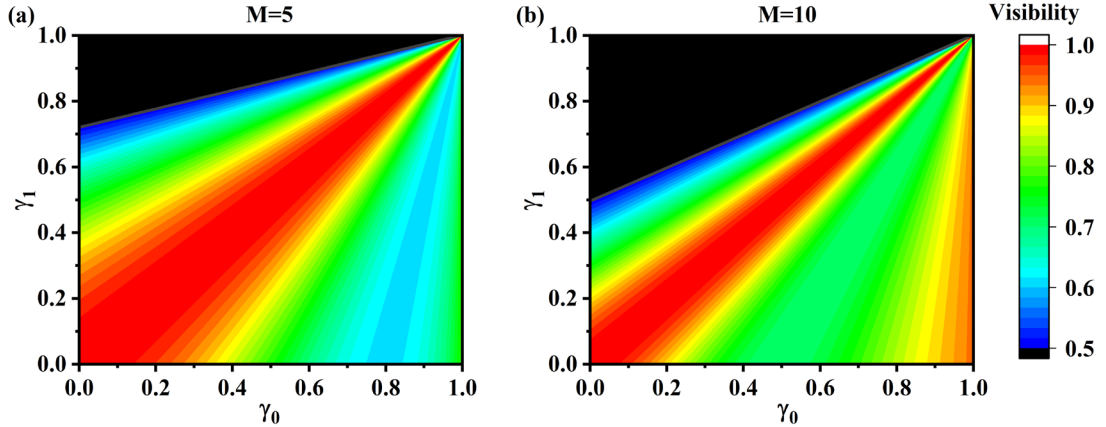


Fig. 5 Visibility versus optical loss probabilities  $\gamma_0$  and  $\gamma_1$  with (a)  $M=5$  and (b)  $M=10$ .

### Conclusion:

We present an interaction-free ghost imaging scheme based on a thermal light source, featuring three key advantages. First, by eliminating the need for quantum light sources and single-photon detectors, it effectively overcomes inherent limitations such as difficulties in quantum state preparation, susceptibility to decoherence, and low detection efficiency. Second, the chain interferometer structure in the signal path not only reutilizes photons that would otherwise be absorbed in conventional schemes to improve image quality, but also induces a quantum Zeno-like effect that significantly reduces optical damage—thereby making the sample nearly immune to light-induced damage as  $M$  increases. This reduction in light-induced damage enables a safe and substantial increase in measurement repetitions, thereby significantly enhancing image quality. Third, we reveal that optical loss in the chain structure can serve as an effective means to regulate background noise, ensuring that the CNR of our scheme is always higher than that of traditional thermal ghost imaging. Our work provides an alternative technical pathway for high-quality, low-damage, and cost-effective imaging by safely utilizing far more photons for imaging than conventional methods—particularly suitable for applications involving light-sensitive objects.

**Data availability:**

All data generated or analyzed during the simulations of study are available from the corresponding author on reasonable request.

**Code availability:**

The code employed to generate the simulations presented in this work is available upon request. Interested parties may inquire about access to the code by contacting the corresponding author.

**Acknowledgements:**

This work is sponsored by Natural Science Foundation of Shanghai (Grant Nos. 25ZR1401140 and 25ZR1401114). This work is also supported by National Natural Science Foundation of China (Grant No. 62161038).

**Author contributions:**

The theory was conceived by Z-H.L. Numerical calculations were performed by S. L. and J.-Y. X.F. under the supervision of Z-H.L. and M.A. All the authors participated in the manuscript preparation, discussions, and checks of the results.

**Corresponding authors:**

Correspondence to Zheng-Hong Li or M. Al-Amri.

**Competing interests:**

The authors declare no competing interests.

**Reference:**

- [1] H. Defienne, W. P. Bowen, M. Chekhova, G. B. Lemos, D. Oron, S. Ramelow, N. Treps and Daniele Faccio, *“Advances in quantum imaging”*, Nat. Photonics **18**, 1024 (2024).
- [2] D. P. Ryan and J. H. Werner, *“A review of quantum imaging methods and enabling technologies”*, Mater. Today Quant. **6** 100044 (2025).
- [3] D. Strekalov, A. Sergienko, D. Klyshko, and Y. Shih, *“Observation of two-photon “ghost” interference and diffraction”*, Phys. Rev. Lett. **74**, 3600 (1995).
- [4] T. B. Pittman, Y. Shih, D. Strekalov, and A. V. Sergienko, *“Optical imaging by means of two-*

*photon quantum entanglement*", Phys. Rev. A **52**, R3429 (1995).

[5] D. P. Ryan, K. Meier, K. Seitz, D. Hanson, D. Morales, D. M. Palmer, B. Hanson, P. M. Goodwin, R. Newell, R. M. Holmes, D. Thompson, and J. Werner, "*Infrared quantum ghost imaging of living and undisturbed plants*", Optica **11**, 1261 (2024).

[6] M. N. O'Sullivan, K. W. C. Chan, and R. W. Boyd, "*Comparison of the signal-to-noise characteristics of quantum versus thermal ghost imaging*", Phys. Rev. A **82**, 053803 (2010).

[7] R. h. Hadfield, "Single-photon detectors for optical quantum information applications." Nat. Photonics, **3**, 696 (2009).

[8] R. H. Dicke, "*Interaction-free quantum measurements: A paradox?*" Am. J. Phys. **49**, 925 (1981).

[9] A. C. Elitzur and L. Vaidman, "*Quantum mechanical interaction-free measurements*", Foundations Phys. **23**, 987 (1993).

[10] P. G. Kwiat, H. Weinfurter, T. Herzog, A. Zeilinger, and M. A. Kasevich, "*Interaction-free measurement*", Phys. Rev. Lett. **74**, 4763 (1995).

[11] A. Agarwal, K. K. Berggren, Y. J. van Staaden, and V. K. Goyal, "*Reduced damage in electron microscopy by using interaction-free measurement and conditional reillumination*", Phys. Rev. A **99**, 063809 (2019).

[12] A. E. Turner, C. W. Johnson, P. Kruit and B. J. McMorran, "*Interaction-free measurement with electrons*", Phys. Rev. Lett. **127**, 110401 (2021).

[13] S. Dogra, J. J. McCord, and G. S. Paraoanu, "*Coherent interaction-free detection of microwave pulses with a superconducting circuit*", Nat. Commun. **13**, 7528 (2022).

[14] V. Vujnović, N. Kralj and M. Karuza, "*Detection of a semitransparent object with no exchange of quanta*", Opt. Express **13**, 1385 (2025).

[15] P. G. Kwiat, A. White, J. Mitchell, O. Nairz, G. Weihs, H. Weinfurter, and A. Zeilinger, "*High-efficiency quantum interrogation measurements via the quantum zeno effect*", Phys. Rev. Lett. **83**, 4725 (1999).

[16] O. Hosten, M. T. Rakher, J. T. Barreiro, N. A. Peters, and P. G. Kwiat, "*Counterfactual quantum computation through quantum interrogation*", Nature **439**, 949 (2006).

[17] H. Salih, Z.-H. Li, M. Al-Amri, and M. S. Zubairy, "*Protocol for direct counterfactual quantum communication*", Phys. Rev. Lett. **110**, 170502 (2013).

[18] X.-S. Ma, X. Guo, C. Schuck, K. Y. Fong, L. Jiang, and H X. Tang, "*On-chip interaction-free measurements via the quantum Zeno effect*", Phys. Rev. A **90**, 042109 (2014).

[19] Y. Cao, Y.-H. Li, Z. Cao, J. Yin, Y.-A. Chen, H.-L. Yin, T.- Y . Chen, X.-F. Ma, C.-Z. Peng,

and J.-W. Pan, “*Direct counterfactual communication via quantum Zeno effect*”, Proc. Natl. Acad. Sci. **114**, 4920 (2017).

[20] C. Liu, J.-H. Liu, J.-X. Zhang, and S.-Y. Zhu, “*The experimental demonstration of high efficiency interaction-free measurement for quantum counterfactual-like communication*”, Sci. Rep. **7**, 10875 (2017).

[21] D. R. M. Arvidsson-Shukur, A. N. O. Gottfries, and C. H. W. Barnes, “*Evaluation of counterfactualty in counterfactual communication protocols*”, Phys. Rev. A **96**, 062316 (2017).

[22] Y. Aharonov, and D. Rohrlich, “*What is nonlocal in counterfactual quantum communication?*”, Phys. Rev. Lett. **125**, 260401 (2020).

[23] J.-K. Li, K. Sun, Y. Wang, Z.-Y. Hao, Z.-H. Liu, J. Zhou, X.-Y. Fan, J.-L. Chen, J.-S. Xu, C.-F. Li and G.-C. Guo, “*Experimental demonstration of separating the wave-particle duality of a single photon with the quantum Cheshire cat*”, Light Sci. Appl. **12**, 18 (2023).

[24] Z.-H. Li, S.-Y. Feng, M. Al-Amri, and M. S. Zubairy, “*Direct counterfactual quantum-communication protocol beyond a single-photon source*”, Phys. Rev. A **106**, 032610 (2022).

[25] G.-C. Guo, and B.-S. Shi, “*Quantum cryptography based on interaction-free measurement*”, Phys. Lett. A **256**, 109 (1999).

[26] T.-G. Noh, “*Counterfactual Quantum Cryptography*”, Phys. Rev. Lett. **103**, 230501 (2009).

[27] Q. Guo, L.Y. Cheng, L. Chen, H. F. Wang, and S. Zhang, “*Counterfactual quantum-information transfer without transmitting any physical particles*”, Sci. Rep. **5**, 8416 (2015).

[28] Z.-H. Li, M. Al-Amri, and M. S. Zubairy, “*Direct counterfactual transmission of a quantum state*”, Phys. Rev. A **92**, 052315 (2015).

[29] Y.-B. Li, S.-W. Xu, Q.-L. Wang, F. Liu, and Z.-J. Wan, “*Quantum key distribution based on interferometry and interaction-free measurement*”, Int. J. Theor. Phys. **55**, 98 (2016).

[30] Y.-Y. Chen, X.-M. Gu, D. Jiang, L. Xie, and L.-J. Chen, “*Tripartite counterfactual entanglement distribution*”, Opt. Express **23**, 21193 (2015).

[31] Q. Guo, L.-Y. Cheng, H.-F. Wang, and S. Zhang, “*Counterfactual entanglement swapping enables high-efficiency entanglement distribution*”, Opt. Express **26**, 27314 (2018).

[32] F. Zaman, Y. Jeong, and H. Shin, “*Dual quantum Zeno superdense coding*”, Sci. Rep. **9**, 11193 (2019).

[33] Z. Cao, “*Counterfactual universal quantum computation*”, Phys. Rev. A **102**, 052413 (2020).

[34] Z.-H. Li, F. Yu, Z.-Y. Li, M. Al-Amri, and M. S. Zubairy, “*Method to deterministically generate large-amplitude optical cat states*”, Commun. Phys. **7**, 134 (2024).

[35] S. Thomas, C. Kohstall, P. Kruit, and P. Hommelhoff, “*Semitransparency in interaction-free measurements*”, Phys. Rev. A **90**, 053840 (2014).

[36] C. Liu, X.-F. Yang, L.-J. Cui, S.-M. Zhou, and J.-X. Zhang, “*Accurate measurement method for refractive index in a high efficiency interaction-free measurement system*”, Opt. Express **28**, 21916 (2020).

[37] Z.-H. Li, L.-J. Wang, J.-P. Xu, Y.-P. Yang, M. Al-Amri, and M. S. Zubairy, “*Counterfactual Trojan horse attack*”, Phys. Rev. A **101**, 022336 (2020).

[38] Y. Chen, Y.-J. Cai, X.-T. Li, K. Huang, J.-M. Liu, and E. Wu, “*Interaction-free quantum spectroscopy*”, Adv. Photonics Res. **2**, 2000206 (2021).

[39] A. M. Pălici, T.-A. Isdrailă, S. Ataman, and R. Ionicioiu, “*Interaction-free imaging of multipixel objects*”, Phys. Rev. A **105**, 013529 (2022).

[40] Y.-Q. Yang, H. Liang, X.-Z. Xu, L.-J. Zhang, S.-N. Zhu, and X.-S. Ma, “*Interaction-free, single-pixel quantum imaging with undetected photons*”, npj Quantum Inf. **9**, 2 (2023).

[41] Y. Zhang, A. Sit, F. Bouchard, H. Larocque, F. Grenapin, E. Cohen, A. C. Elitzur, J. L. Harden, R. W. Boyd, and E. Karimi, “*Interaction-free ghost-imaging of structured objects*”, Opt. Express **27**, 2212 (2019).

[42] S. Ahmadi, E. Saglamyurek, S. Barzanjeh and V. Salari, “*High-contrast interaction-free quantum imaging method*”, Phys. Rev. A **107**, 032611 (2023).

[43] J. R. Hance and J. Rarity, “*Counterfactual ghost imaging*”, npj Quantum Inf. **7**, 1 (2021).

[44] Peiming Li, Xiaojin Chen, Xiaodong Qiu, Binglin Chen, Lixiang Chen, Baoqing Sun, “*Ghost imaging, development, and recent advances [Invited]*”, Chin. Opt. Lett. **22**, 112701 (2024).

[45] A. Forbes and F. Nothlawa, “*How a thirty-year-old quantum tale of two photons became ghost imaging*”, Commun. Phys **8**, 174 (2025).

[46] A. Valencia, G. Scarcelli, M. D'Angelo, and Y. Shih, “*Two-Photon Imaging with Thermal Light*”, Phys. Rev. Lett. **94**, 063601 (2005).

[47] D. Zhang, Y.-H. Zhai, L.-A. Wu, and X.-H. Chen, “*Correlated two-photon imaging with true thermal light*”, Opt. Lett. **30**, 2354 (2005).

[48] R. S. Bennink, S. J. Bentley, and R. W. Boyd, “*“two-photon” coincidence imaging with a classical source*”, Phys. Rev. Lett. **89**, 113601 (2002).

[49] A. Gatti, E. Brambilla, M. Bache, and L. A. Lugiato, “*Ghost imaging with thermal light: comparing entanglement and classical correlation*”, Phys. Rev. Lett. **93**, 093602 (2004).

[50] K. W. C. Chan, M. N. O'Sullivan, and R. W. Boyd, “*Optimization of thermal ghost imaging: high-order correlations vs. background subtraction*”, Opt. Express **18**, 5562 (2010).

[51] J. H. Shapiro, “*Computational ghost imaging*”, Phys. Rev. A. **78**, 061802 (2008).

[52] Y. Bromberg, O. Katz and Y. Silberberg, “*Ghost imaging with a single detector*”, Phys. Rev. A. **79**, 053840 (2009).

[53] B. I. Erkmen and J. H. Shapiro, “*Ghost imaging: from quantum to classical to computational*”, Adv. Opt. Photonics **2**, 405 (2010).

[54] D.-X. Zhou, H.-Z. Zhang, H.-Y. Yu, G.-Q. Zhang, “*High-visibility calculating ghost imaging with self-reconstruction capability and extendible depth-of-field*”, Opt. Express **12**, 30076 (2024).

[55] H. Wu, B. Hu, L. Chen, F. Peng, Z.-N Wang, G. Genty and H.-K. Liang, “*Mid-infrared computational temporal ghost imaging*”, Light Sci Appl **13**, 124 (2024).

[56] K. Li, W.-J. Zhou, X.-P.-F. Zou, X. Liu, Y.-N. Yi, Q. Fu, X.-W. Huang, Y.-F. Bai and X.-Q. Fu, “*Three-dimensional computational ghost imaging with only single-pixel detection based on deep learning preprocessing pseudo-thermal light*”, Opt. Laser Technol. **92**, 113680 (2025).

[57] J.-T. Xie, H. Zeng, M.-F. Li, Y.-F. Li, J.-G. Wang, B.-G. Quan, L.-M. Chen, and L.-A. Wu, “*Fast X-ray ghost imaging by scanning aggregate patterns*”, Photonics Res. **13** 2734 (2025).

[58] Z.-B. Hou, J.-F. Tang, C.-J. Huang, Y.-F. Huang, G.-Y. Xiang, C.-F. Li, and G.-C. Guo, “*Entangled-State Time Multiplexing for Multiphoton Entanglement Generation*”, Phys. Rev. Appl. **19**, L011002 (2023).

[59] A. Gatti, E. Brambilla, M. Bache, and L. A. Lugiato, “*Correlated imaging, quantum and classical*”, Phys. Rev. A **70**, 013802 (2004).

[60] F. Ferri, D. Magatti, A. Gatti, M. Bache, E. Brambilla, and L. A. Lugiato, “*High-Resolution Ghost Image and Ghost Diffraction Experiments with Thermal Light*,” Phys. Rev. Lett. **94**, 183602 (2005).

[61] G. Scarcelli, V. Berardi, and Y. Shih, “*Can Two-Photon Correlation of Chaotic Light Be Considered as Correlation of Intensity Fluctuations?*” Phys. Rev. Lett. **96**, 063602 (2006).

[62] R. Meyers, K. S. Deacon, and Y. H. Shih, “*Ghost-imaging experiment by measuring reflected photons*,” Phys. Rev. A **77**, 041801(R) (2008).

[63] Supplementary Notes.

[64] L. Mandel and E. Wolf, “*Optical Coherence and Quantum Optics*”, (Cambridge University Press, New York, 1995).